

**Supporting Information For:**

**Coupling of Plasmonic Hot Spots with Shurikens for Superchiral SERS-based Enantiomer Recognition**

*Olga Guselnikova\**,<sup>1,3</sup> *Roman Elashnikov*,<sup>1</sup> *Vaclav Svorcik*,<sup>1</sup> *Martin Kartau*,<sup>2</sup> *Cameron Gilroy*,<sup>2</sup> *Nikolaj Gadegaard*,<sup>4</sup> *Malcolm Kadodwala*,<sup>2</sup> *Affar S. Karimullah\**,<sup>2</sup> *Oleksiy Lyutakov\**<sup>1</sup>

<sup>1</sup> Department of Solid State Engineering, University of Chemistry and Technology, 16628 Prague, Czech Republic

<sup>2</sup> School of Chemistry, Joseph Black Building, University of Glasgow, Glasgow, G12 8QQ, UK.

<sup>3</sup> Research School of Chemistry and Applied Biomedical Sciences, Tomsk Polytechnic University, Tomsk, 634050, Russian Federation

<sup>4</sup> James Watt School of Engineering, Rankine Building, University of Glasgow, Glasgow, G12 8LT, UK

Table of content:

**CONTENTS**

---

1. Experimental part.....	2
2. Shurikens structures .....	5
3. Simulations of shurikens optical response.....	8
4. Additional silver nanoclusters array deposition.....	10
5. Control experiments – R6G response on Si, Ag/Si, and S3/Au substrates under 785 nm excitation.	13
6. Plasmonic coupling between Au shurikens and Ag nanostructures.....	15
7. Cysteine enantiomers deposition and measurements.....	17
8. SERS probe wavelength proof of Ag – shuriken plasmonic coupling.....	23
9. Analysis of mixtures and SERS substrate re-utilization.....	24
10. Biomolecules experiments – DNA case.....	26
References .....	28

## 1. EXPERIMENTAL PART

---

**1.1 Preparation of Au Shurikens.** The templated substrates were prepared by injection moulding. Clean silicon substrates were coated with  $\sim 80$  nm of PMMA (Elvacite 2041, Lucite International) and exposed in a Vistec VB6 UHR EWF lithography tool operating at 100 kV. After exposure, the substrates were developed and a 300  $\mu\text{m}$  thick nickel shim was formed through electroplating. The shim was then mounted in a custom-made tool, capable of manufacturing ASA standard polymer slides. An Engel Victory Tech 28 tons injection moulding machine was used in fully automatic production mode in the manufacture of polymer slides using polycarbonate (Makrolon DP2015) as feedstock. The injection moulded substrates have chiral nanostructures imparted in the plastic surface and was subsequently covered by a continuous 100 nm Au film to complete the TPS process.

**Deposition of Ag.** Silver was deposited onto gold-coated Shurikens by a vacuum sputtering method (DC Ar plasma, gas purity – 99.995%, gas pressure 4 Pa, discharge power 7.5 W, sputtering time 50-250 s). Ag target for metal deposition (purity of metal 4 N) was purchased from Safina.

**1.2 Surface characterization techniques.** SEM and SEM-EDX measurements were carried out using accelerating voltages 10 and 2 kV, respectively (Oxford Instruments). Alternatively, for characterization of the sample surface, the peak force AFM technique was applied. Surface mapping was performed with Icon (Bruker) set-up on the areas of  $3 \times 3 \mu\text{m}^2$  and  $200 \times 200 \text{ nm}^2$ . AFM scratch tests were carried out by profiling across a scratch (created with steel tweezers lightly pressed against the sample surface) at an angle of  $90^\circ$  relative to the surface (for the scratch tests, the glass substrates with thin Au layer were used as supports for Ag deposition). To determine the Ag thickness, measurements were taken each time on three samples, at nine locations on each sample. The Ag thickness was then calculated as the average increase in the thickness of the metal layer(s).

**1.3 Measurements of optical spectra.** A custom built polarimeter, equipped with a tungsten halogen light source (Thorlabs), polarisers (Thorlabs), and a  $10\times$  objective (Olympus) was used for measurements of reflection spectra. The samples are positioned with the help of a camera (Thorlabs, DCC1645C) and the spectrum was measured using a compact spectrometer (Ocean optics USB4000). Reflectivity measurements used plain Au as a background. ORD spectra were obtained using the Stokes' method. Briefly, linearly polarised light was incident

on the substrate and the intensities of reflected light at four polarisation angles (0,  $\pm 45$  and  $90^\circ$ ) relative to the incident are measured. The errors were determined from the deviation of 8 measurements.

**Raman measurement.** Raman spectra (except the wavelength-dependent measurements) were recorded using a ProRaman-L spectrometer (785 nm and 15 mW power) with 1 averaging and 100 s accumulation time. Thermo Scientific DXR Raman Microscope (532 nm and 1 mW power) was used for wavelength-dependent measurements with 1 averaging and 100 s accumulation time. Renishaw inVia Reflex Raman Microscope (633 nm and 5 mW power, 830 nm and 25 mW power) was used for wavelength-dependent measurements with 1 averaging and 100 s accumulation time. Excitation and collection of Raman scattered light was done using a  $40\times$  objective. From each sample, 10 random points were analysed on each shuriken array. For each sample, the average intensity value was calculated. All spectra were baseline corrected and smoothed using an 11-point averaging smoothing algorithm to reduce the baseline variability in the region between  $450 - 2000 \text{ cm}^{-1}$ , using Omnic Professional Software Suite (Thermo Scientific, Inc., Madison, WI). For Raman mapping, the spectra collection across the surface area of  $0.25\times 0.25 \text{ mm}^2$  (for DNA) and  $0.85\times 0.45 \text{ mm}^2$  (for cysteine) was performed and characteristic SERS band intensities were interpolated using Clough–Tocher method.

**Reusability of SERS substrates.** After the sensing of cysteine, the freshly prepared RH- and LH-S3/Ag samples were immersed in 15 mL of methanol for 1 hour and then treated with ultrasound for 30 sec. (35 kHz, SONOPULS mini20) followed by drying in the air. The fresh  $10^{-6} \text{ M}$  solution of L/D-cysteine was deposited on dry substrates and subjected to SERS measurements. The procedure was repeated several times with different time intervals between samples regeneration and re-utilization.

**EF calculation.** Calculation of SERS EF was performed according to the standard relation:  $EF = \frac{I_{SERS}/C_{SERS}}{I_{RS}/C_{RS}}$ , where the  $I_{SERS}$  and  $I_{RS}$  represent the Raman scattering intensities on SERS-active and reference silicon surfaces, and  $C_{SERS}$  and  $C_{RS}$  are the corresponding molar concentration of R6G.

$N_{SERS}$  was calculated considering that R6G is deposited homogeneously over the square sample. The calculations were performed taking into account laser spot and calculated height of deposited R6G

$$N_{SERS} = \frac{\pi * R_{laser}^2 * n_{drop}}{L_{sample}^2} * N_A$$

Where,  $R_{laser}$  is the radius of laser spot (15  $\mu\text{m}$ ),  $n_{drop}$  number of molecules in the deposited drop,  $L_{sample}$  is the size of square sample (0.7 cm),  $N_A$  is the Avogadro constant

$$N_{SERS} = 2.8 * 10^{-16} \text{mol}$$

20  $\mu\text{L}$  of the R6G solution was dropped on the substrate. The drop spread spontaneously into a circle of about 3 mm in diameter after the solvent evaporated.

For the calculation of  $N_{RS}$ , all parameters were the same as described for  $N_{SERS}$ ,  $L_{sample}$  is the size of square sample (0.4 cm). Using the same approach,  $N_{RS} = 3.63 * 10^{-13} \text{mol}$ .

**DNA hybridization and measurement.** For the hybridization experiments, annealing buffer (10 mM Tris, pH 7.5, 50 mM NaCl, 1 mM EDTA) was used. Oligonucleotide (5'-CGCCAATACGACCAAATCCG-3) at concentration  $5 \times 10^{-9}$  M, 1 ml (annealing buffer) was mixed with 1 ml of complimentary oligonucleotide at  $5 \times 10^{-9}$  M (5'-CGGATTTGGTCGTATTGGCG-3). The resulting solution in a plastic beaker of 3 ml volume was heated to 90°C on a block heater (Thermo Scientific™) for 2 min and then gradually (1.5°C per minute) cooled to 25°C. Afterward, 100  $\mu\text{l}$  of DNA solution was drop deposited on Sx/Ag surface and left in the refrigerator until completely dry. Raman spectra were recorded with 40 mW laser power and accumulation time 200 s.

**Preparation and grafting of molecular temperature probe of ADT-C $\equiv$ N and its grafting.** For surface modification, the diazonium salt, 4-cyanobenzenediazonium tosylate (ADT-CN), was synthesized according to the previously developed route.<sup>S1</sup> RH/LH-S3/Ag samples were immersed in 1mM solution of ADT-CN for 1 hour with further washing by water and methanol and dried under vacuum.

**Local heating estimation.** For estimation of local surface heating, which occurred due to sample illumination during SERS measurement, the molecular probe (-C<sub>6</sub>H<sub>4</sub>-CN) was used. First, the temperature-induced shift of the characteristic CN band position was monitored using the substrate external heating (controlled by an ultrathin thermocouple attached to the sample surface). The external heating was performed from room temperature (RT) up to 65°C temperature range with a 1 °C/min heating rate. Then, SERS measurements of the molecular probe were performed at RT (5x at the same laser spot with a negligible pause between

measurements). Comparison of CN band position shift occurred due to external heating and due to Raman laser illumination allows us to estimate the local surface temperature.

**Simulations:** Simulations were performed using COMSOL v5.6, a software for simulating physics using finite element method. Periodic boundary conditions were used to emulate the array of nanostructures. Perfectly matched layer conditions were used above and below the input and output ports. Linearly polarized EM wave was applied at normal incidence onto the structure.

## 2. SHURIKENS STRUCTURES

---

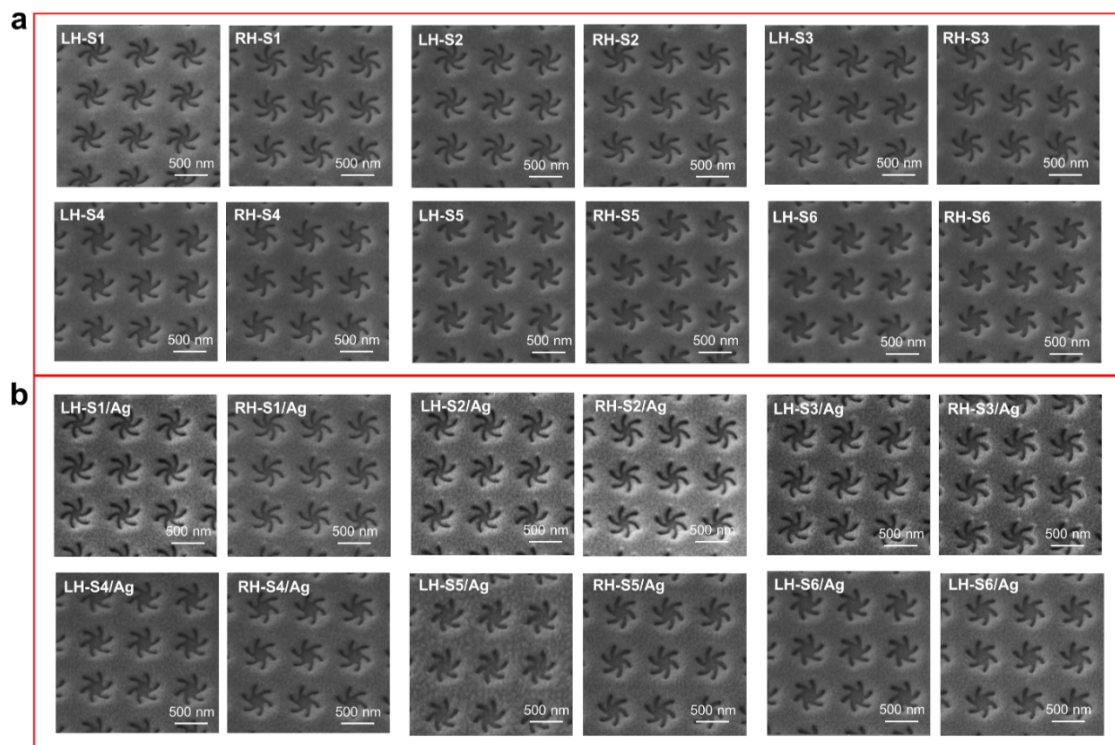


**Fig. S1** (a) - SEM images of pristine shurikens (gold covered structures, further designated as S1-S6), (b) – corresponded shurikens structures after Ag layer deposition (1.3 effective thickness).

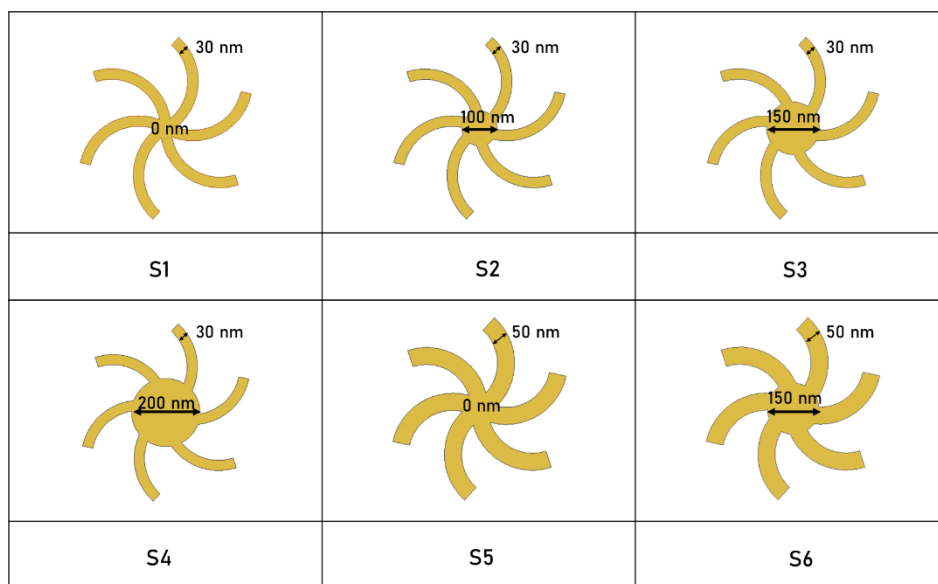


**Fig. S2 (a)** - schematic description of shuriken(s) morphology and difference between S1-S6;

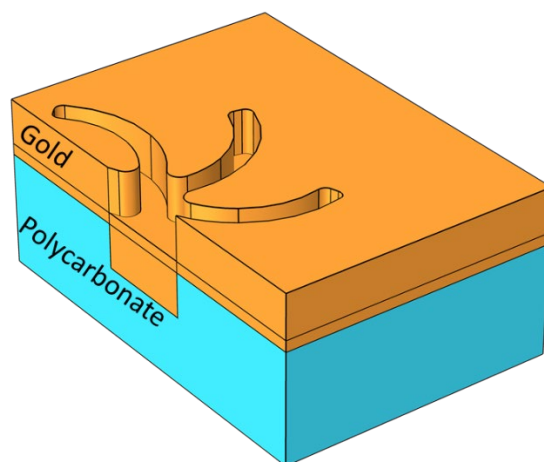


**Fig. S3** cross-section of templated shuriken nanostructure showing gold film and polycarbonate base.

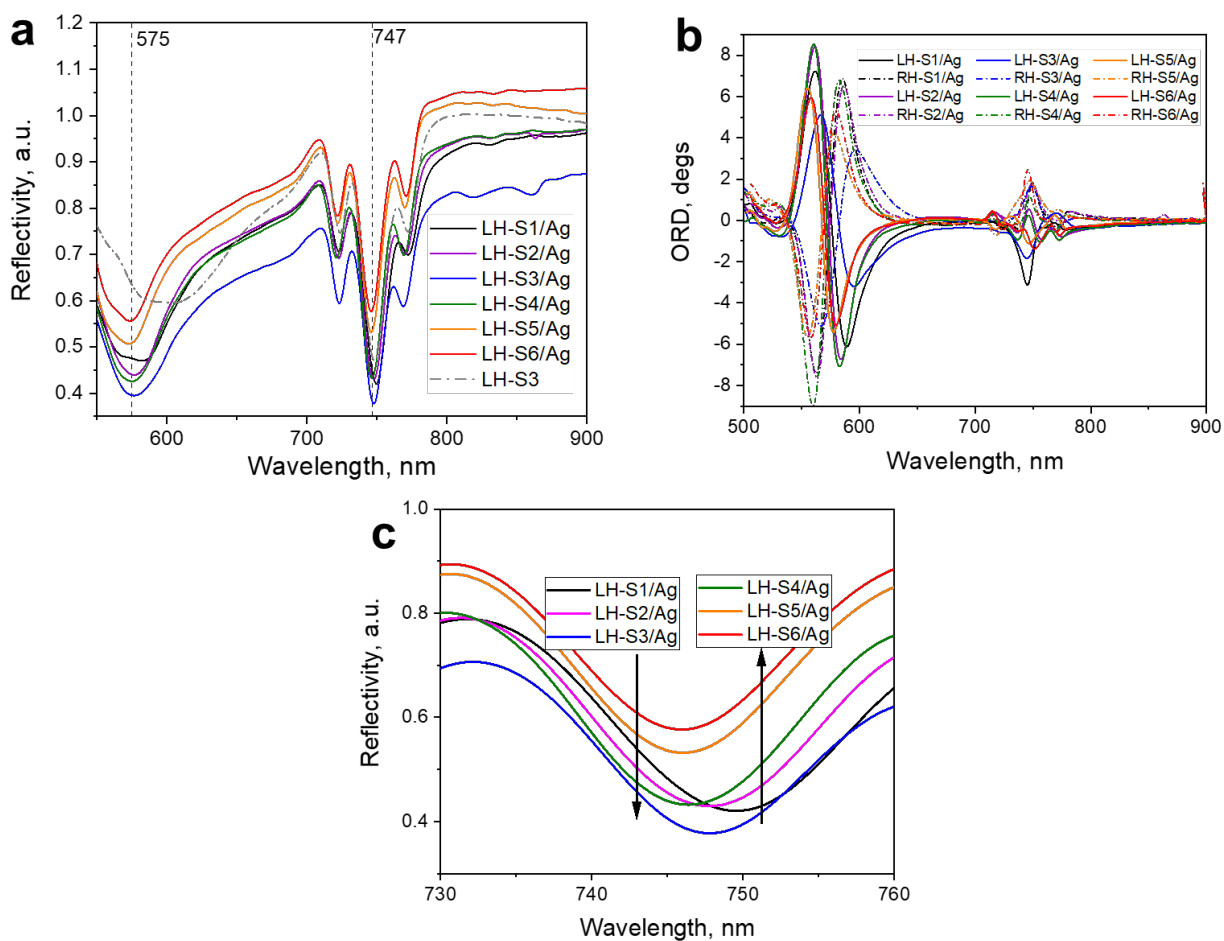


**Fig. S4** (a) - reflectivity and (b) - optical rotation dispersion for Sx/Ag structures (measurements performed in air); (c) - detail of the drop of reflected light intensity, corresponding to plasmon excitation on Sx/Ag structures (dependence of plasmon excitation efficiency on initial shuriken geometry is designated by arrows).

### ***The geometry of RH/LH-S1-6/Ag***

Gold shurikens SEM photos (right or left handed: RH or LH) are presented in Fig. S1a and schematical representation is on Fig. S2. Each nanostructure varies in two parameters in their initial master shim (used for injection moulding) design – arm width and diameter of a circle in the middle of shuriken (see Figs. S1-S4). The first parameter is the arm widths (Fig. S2) and the second parameter is the diameter of a circle added in the middle of the shuriken to enlarge its center. The differences in optical response due to these parameters are very subtle (Fig. S4). The periodic pattern consists of chiral shuriken-shaped indentations of either LH or RH

handedness, arranged in a square lattice with 720 nm periodicity. The depth of the indentation was 80 nm, with slightly sloped edges (approximately 30°), while the distance from the end of one arm to that of the end of the opposite arm is 500 nm<sup>S1, S2</sup>. The Au thickness is 100 nm, and along with the slope at the edges, will create an overlap between the metal inside the indentation and the metal at the top, thereby generating a continuous Au film (Fig. S3). As is evident, the main shurikens geometrical parameters are conserved after the Ag deposition. In turn, Fig. S2 highlights the main difference between the shurikens.

### ***Optical properties of RH/LH-S1-6/Ag***

For shurikens itself, the resonance positions are dependent on the lattice pitch which remains constant in all the arrays; however, the arm width and central circle generate very small resonance shifts for the resonance at 747 nm (Fig. S4) and reflectivity is also varying. The effect is manifested by the optical reflectivity spectrum as a function of 1.3 nm Ag layer. The changes in reflectivity after Ag deposition were hardly pronounced for S1/Ag, S2/Ag, and S4/Ag structures as well as for S5/Ag and S6/Ag structures. It should also be noted that the pristine S5 and S6 shurikens structure show less intensive extinction and ORD peaks. Thus, the lower efficiency of these structures in enantioselective discrimination can be expected. In turn, the S3/Ag samples show increased absorption, which will potentially lead to increase in the field strengths generated. Even at these wavelengths, the measurement of optical rotation dispersion (ORD) indicates the appearance of ORD bands with opposite signs and mirror-like symmetry for LH- and RH- samples (Fig. S4b). Hence, the deposition of Ag layer led to the small shift and broadening in the reflection (absorption) spectra plus a decrease in overall reflectivity indicating overall higher absorption by the shurikens arrays, especially pronounced for S3/Ag samples. This indicates that S3/Ag array will likely have a stronger resonance and generate stronger near fields. S3/Ag would hence have a better overlap with 785 nm laser excitation.

### **3. SIMULATIONS OF SHURIKENS OPTICAL RESPONSE.**

---

We simulated the shuriken metafilms for a chiral structure and nanorods displaced in the y direction as a two-dimensional low symmetry structure for comparison<sup>S3</sup>. Fig. S4 shows the reflectivity/transmission of the two structures and plots that represent chirality through the calculated optical chirality (C) value at peak resonance positions and surface with highest intensity of near fields. The C value is calculated by:

$$\bar{C} = \frac{\epsilon_0 \omega}{2} \text{Im}(\mathcal{E}^* \cdot \mathcal{B})$$

The value is then normalized to the C for right circularly polarized (RCP) plane waves propagating in air for the same wavelength.

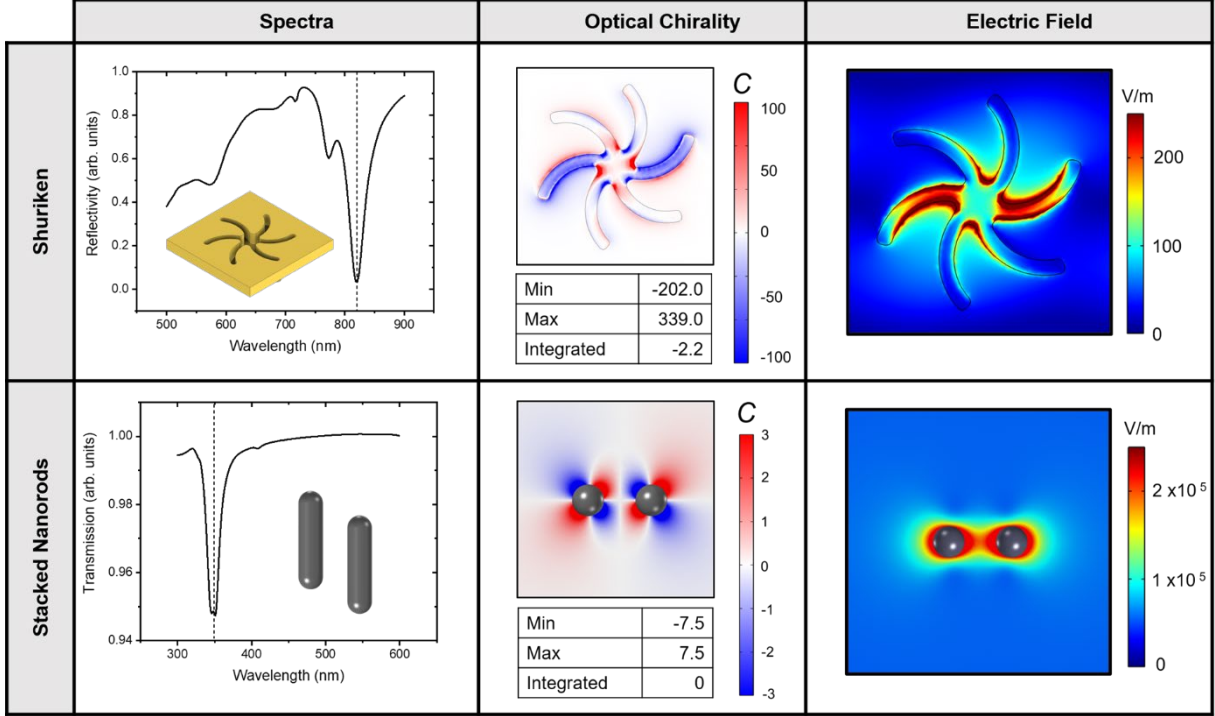


**Fig. S5** Comparison of simulated shurikens (Top) and nanorods (Bottom) generating chiral fields at their peak resonance. The chirality is measured by calculating the normalized C value, and E field intensity, at the top surface of the shuriken metafilm and an x-y plane passing through the center of the nanorods through the highest intensity of near fields. The C value maximum and minimum over the surfaces, and the integrated C values for the surface are presented in the tables.

The shuriken structures show chirality that is roughly two orders of magnitude larger than that for the nanorods. The net C, or integrated value over the surfaces shows the shurikens have a net negative C whereas the less chiral nanorod geometry produces a net zero value.

#### 4. ADDITIONAL SILVER NANOCUSTERS ARRAY DEPOSITION.

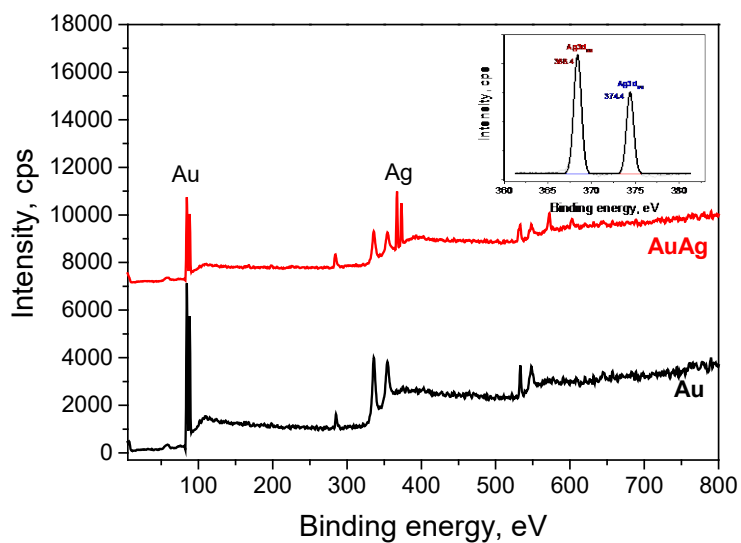


**Fig. S6** XPS spectra, measured on Au shurikens surface before and after deposition of silver (effective thickness – 1.3 nm).

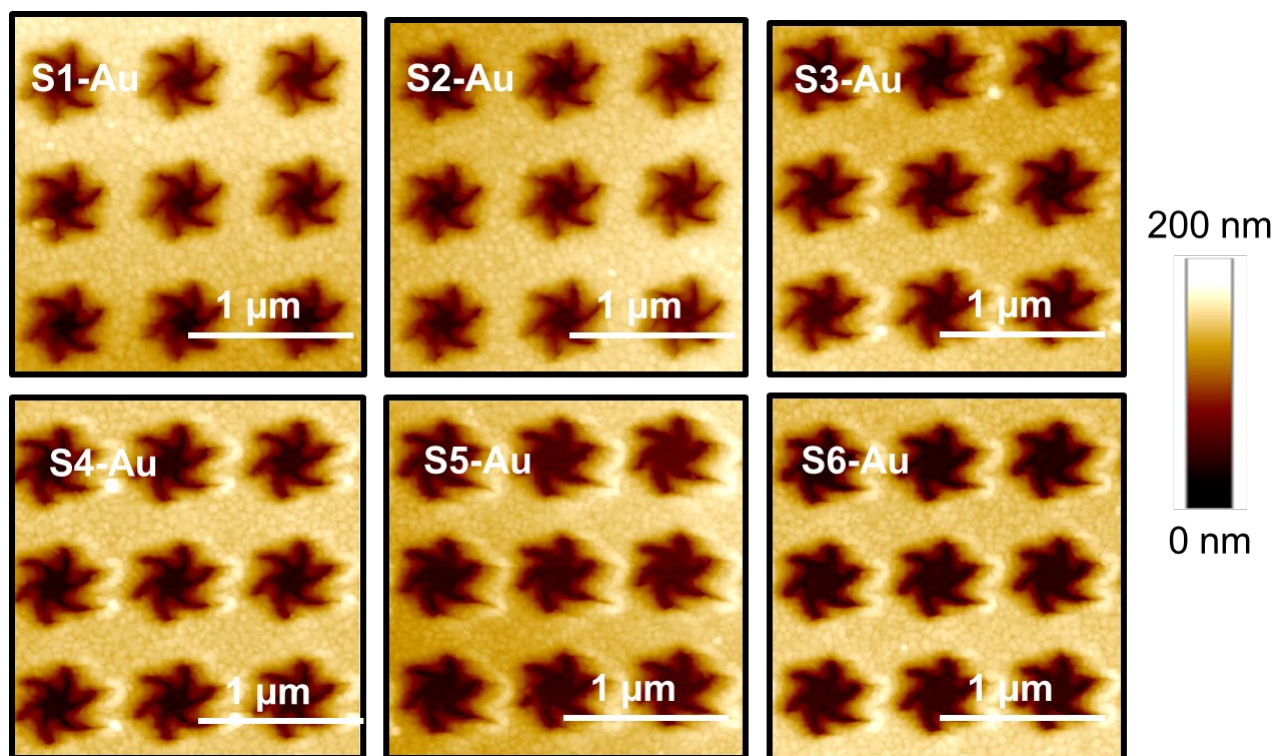


**Fig. S7** AFM images of left-handed Au covered shuriken arrays denoted as S1-6-Au, where S1, S2, S3, S4, S5 and S6 are corresponded to the different geometry of shurikens shown at Fig. S2

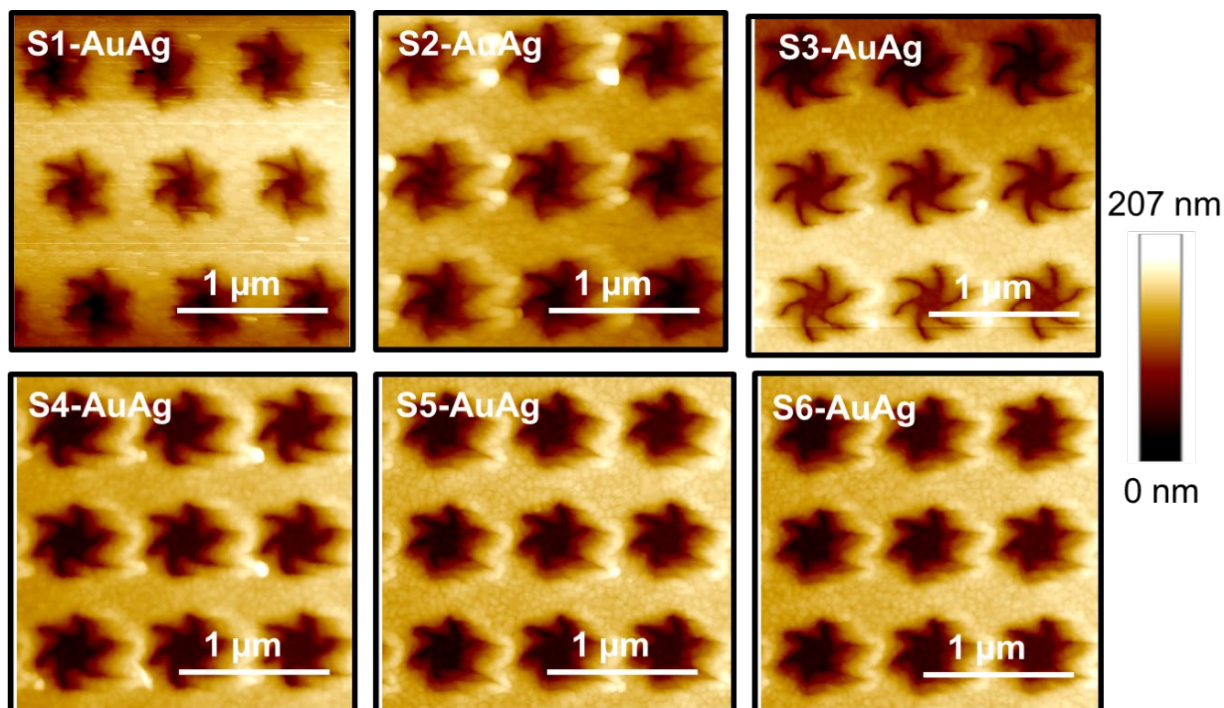


**Fig. S8** AFM images of left-handed Au covered shuriken arrays after Ag sputtering (150 seconds).

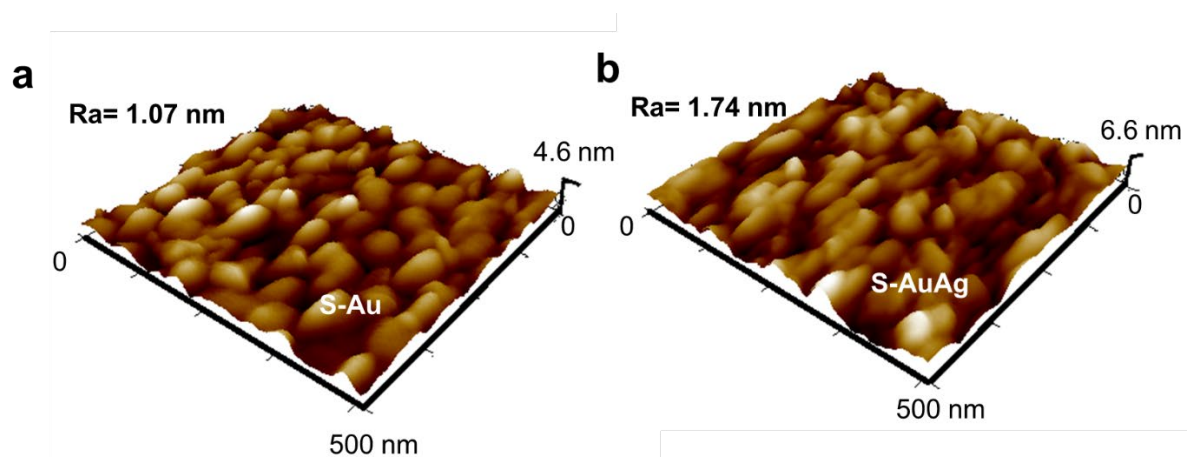


**Fig. S9** (a) AFM images of pristine S3 and (b) S3/Ag (1.3 nm effective thickness) surface morphology, measured inside the shuriken structure.

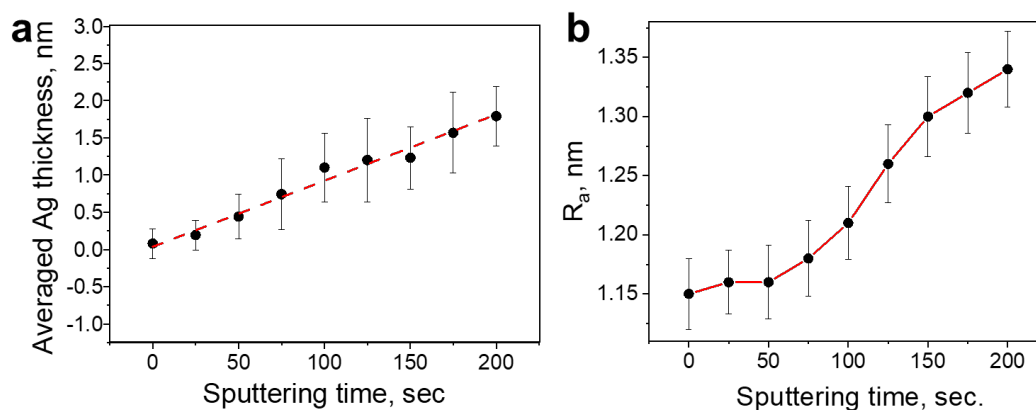


**Fig. S10** For S3/Ag structure: (a) dependency of Ag thickness and (b) surface roughness (measured inside the shuriken structure) as a functions of Ag sputtering time.

***Fig. S6-S10 – related discussion***

Since the pristine Ag shuriken surface does not show a sufficient level of SERs activity, we performed additional Ag nanostructure deposition. The conditions of Ag deposition were chosen to ensure a rather imperfect, cluster-like surface. The presence of silver was confirmed by the XPS measurements, which indicate the appearance of apparent Ag-related peaks (Fig. S6) and by AFM scratch tests (performed on independent samples with glass support), which also shows the gradual increase of Au/Ag “effective” thickness with the increasing of sputtering time. The SEM and AFM images (Fig. S1 and Figs. S7, S8) show the conservation of the overall shurikens geometry after the Ag deposition. However, more detailed AFM scans (performed inside the shuriken structure), indicate the increase of surface roughness (Fig. S9 gives an illustrative example; the general dependency is presented in Fig. S10). Such behaviour, which is accompanied by the increase of apparent Ag thickness, should be attributed to the formation of cluster-like silver structures, which can be approximated as a system of randomly oriented/distributed plasmonic dipoles or hot spots.

**5. CONTROL EXPERIMENTS – R6G RESPONSE ON SI, AG/SI, AND S3/AU SUBSTRATES UNDER 785 NM EXCITATION.**

---

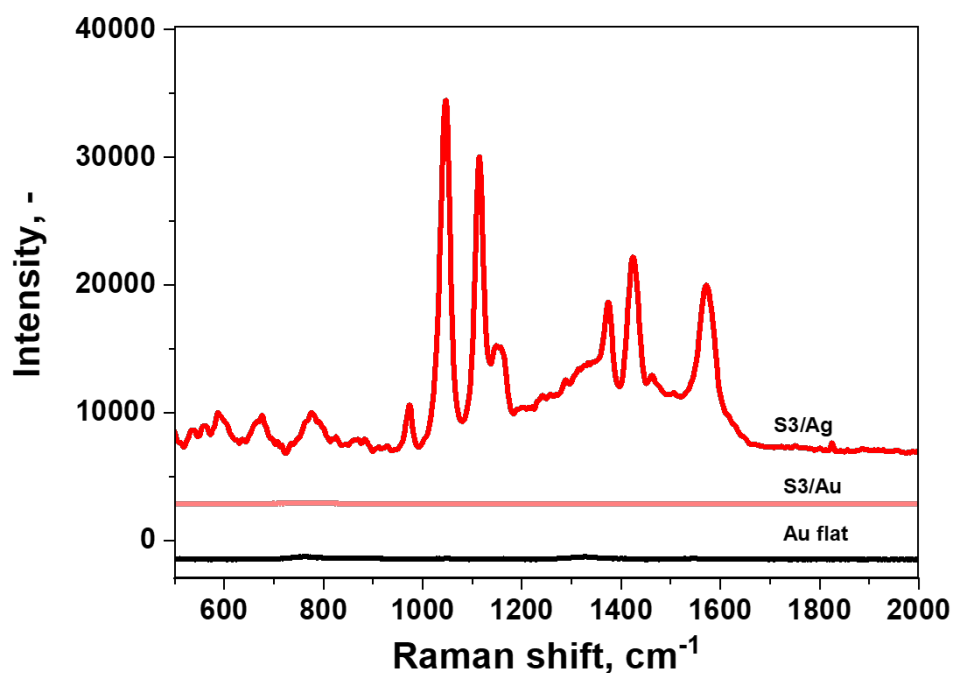


**Fig. S11.** Comparison of SERS spectra of R6G ( $10^{-6}$  M) measured on Au flat surface, S3/Ag and S3/Au (prepared by the sputtering of gold for 150 seconds on S3 shurken).

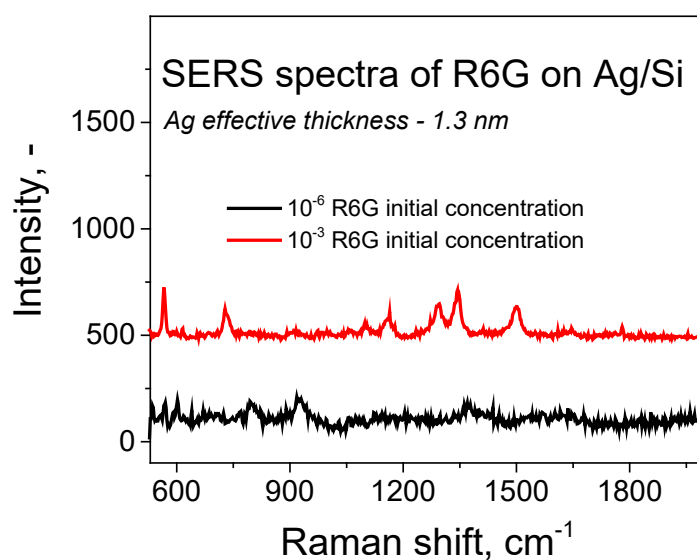


**Fig. S12** SERS spectra of R6G deposited on Ag/Si (with 1.3 nm Ag thickness) at  $10^{-3}$  and  $10^{-6}$  M measured at 785 nm wavelength

**Fig. S11-12 – related discussion.**

The SERS response from R6G molecules on Ag coated shurikens, that is S3/Ag, pristine Au shurikens, S3/Au, and flat Au is shown in Fig. S11. We used the standard R6G solution ( $10^{-6}$ M and  $10^{-3}$ M) and thousand times increased dye concentration ( $10^{-3}$ M). The results indicate that the S3/Ag or the Au shuriken-Ag nanocluster combination has a vast improvement on the SERS enhancement that is unobservable for the pristine Au shurikens and just plain flat Au.

The Raman responses of R6G molecules deposited on Si/Ag surface were also measured in control experiments (to verify the impact of Ag-shurikens coupling). The parameters of Ag layers deposition were tuned to match the shuriken case (in terms of effective Ag thickness and roughness). Obtained SERS spectra are presented in Fig. S12. As could be expected, the lower concentration of R6G deposited on the Si surface does not produce any reasonable Raman signal. Higher dye concentration leads to the appearance of characteristic R6G peaks, but still with low intensity. This result was expected since the silver only layer is not a suitable SERS substrate for excitation at 785 nm wavelength. So, in this way, the key role of shurikens is highlighted - the incident photons have to be first absorbed by shuriken (which have a resonance frequency near 785 nm), and even after this, the Ag hot spots can be excited by shuriken superchiral near field.

#### Additional spectra of R6G on LH-Sx/Ag structures

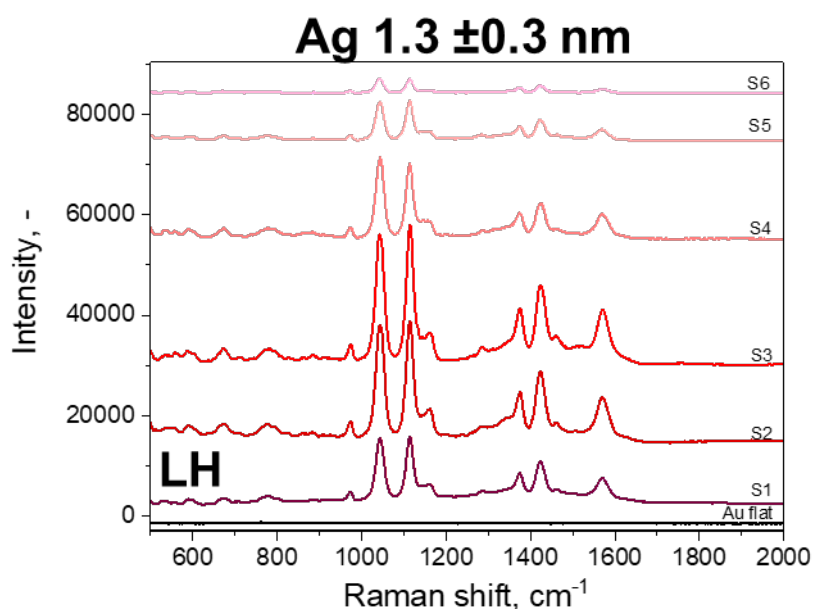


**Fig. S13** SERS spectra of R6G, measured on LH-Sx/Ag structures as a function of shurikens geometry.

## 6. PLASMONIC COUPLING BETWEEN AU SHURIKENS AND AG NANOSTRUCTURES.

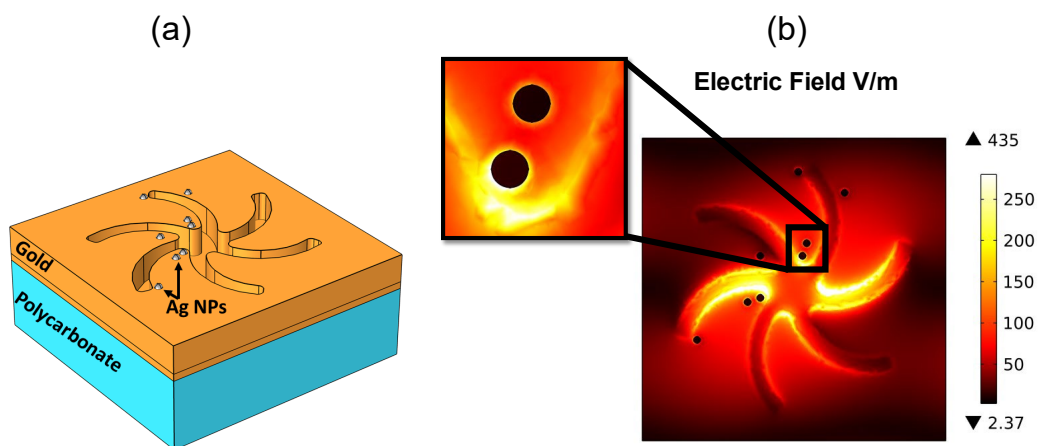
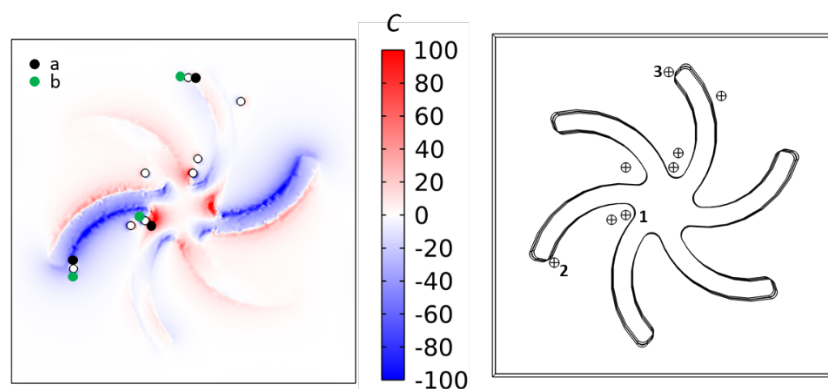


**Fig. S14** (a) - simulation schematic of Ag nano particles on the shuriken surface; (b) - electric field plot of shuriken at 824 nm mode, from a cut plane 5 nm above the shuriken surface. Inset shows two silver nanoparticles effected by strong electric fields near shuriken centre and arms.



z=105		
Normalised C		
	a	b
Point 1	79.0	-23.5
Point 2	-30.4	-15.9
Point 3	4.75	-4.23

**Fig. S15** chirality parameter  $C$  calculated at the surface of shuriken nanostructure ( $z = 105$  nm). Table shows three selected silver nanoparticles (1-3) with normalised  $C$  calculated for a/b regions.

***Figs. S14, S15 – related discussion***

We performed simulations of Ag nano particles (NPs) on the Au shuriken surface. Far-field optical properties (Reflectivity and ORD) had no noticeable difference for such a small amount of Ag. Figure S13 shows the  $|\mathbf{E}|$  field intensity (at plasmon resonance wavelengths) at 5nm above the Au surface cutting through roughly half of the dome shaped nanoparticles which are 10 nm in height. The field intensities show how the nanoparticles couple to the field generated by the shuriken when in close vicinity to the regions where the fields are strongest. Figure S14 shows a comparison of the chirality near 3 nanoparticles numbered 1, 2 and 3. Certain particles have equal and opposite symmetry around them while those close to the shuriken plasmonic hot spots can be overwhelmed by the chiral fields generated by the shuriken and have a net positive or negative chiral field around them. We calculate the chirality factor  $C$  using  $C = -0.5(\epsilon_0 \cdot \omega) \text{Im}(E^* \cdot B)$ , where  $E$  is the electric field and  $B$  the magnetic field, to characterise the chiral fields. The table below shows the normalised  $C$  (with circularly polarised right handed light as the reference) at two opposite points surrounding each particle. Point 1 is in a region of high  $E$  field and chiral fields generated by the shuriken but is under influence of both left and right handed fields. It hence has large values of  $C$  in its surrounding but overall net positive. Point 2 is near the arm end but with strong plasmonic fields again. Here its nature is net negative, and the nanoparticle is surrounded by relatively large chiral fields. Point 3 is in a region where the current mode does not produce strong fields. It does however resonate itself yet generates near zero net chirality. The simulation results highlight how the shuriken chiral behaviour and fields modulate the behaviour of the achiral nanoparticles. If the nanoparticles are the source of the SERS response, the results here show, that the nanoparticle fields generating the SERS are likely to be chiral in nature themselves and this response due to coupling would affect the SERS response from the chiral molecules.

## 7. CYSTEINE ENANTIOMERS DEPOSITION AND MEASUREMENTS.

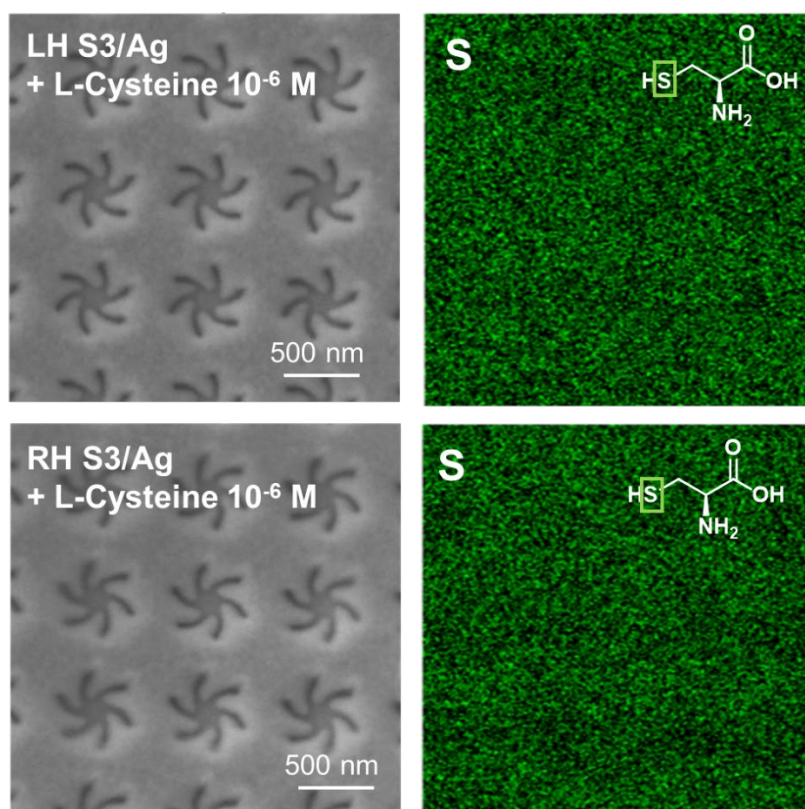


**Fig. S16.** SEM images of LH and RH S3/Ag structures, measured after cysteine spin coating ( $10^{-5}$ M solution) with the corresponding EDX-measured maps of sulphur distribution.

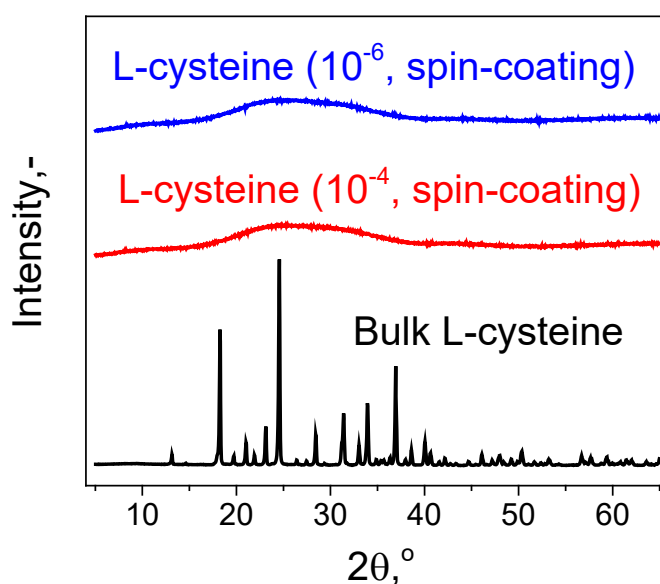


**Fig. S17** XRD spectra of L-cysteine powder and cysteine layer deposited on Au/Ag substrates.

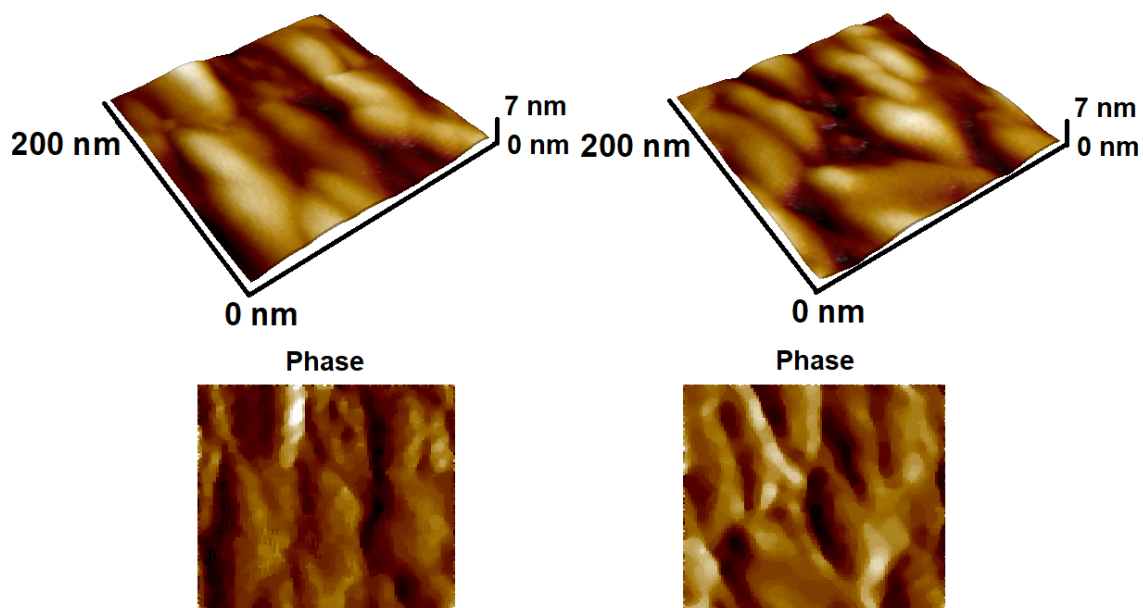


**Fig. S18** Surface morphology and corresponding phase images, measured by AFM “inside” the S3/Ag structure before (left part) and after (right part) cysteine deposition.

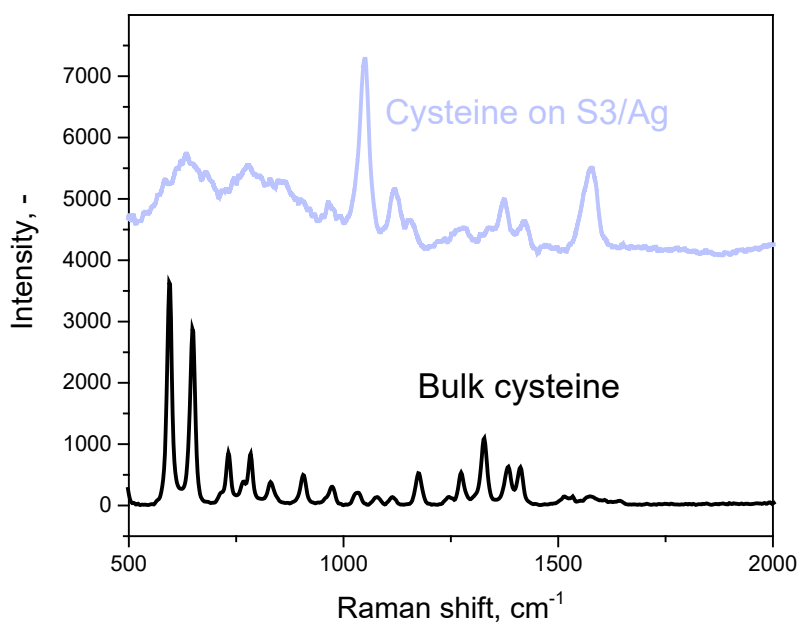


**Fig. S19** Comparison of SERS spectrum, measured on S3/Ag substrates, with Raman one, measured on cysteine powder.

*Fig. S16-S19 – related discussion*

The homogeneity of cysteine layers was firstly evaluated using the EDX mapping (and related SEM measurements). Obtained results are presented in Fig. S16, where the conservation of the overall shuriken structure as well as the homogeneous distribution of sulfur as a “marker” element is well evident. So, the results of EDX mapping confirm the homogeneous distribution of cysteine across the shuriken structure.

The absence of cysteine crystal phase was checked using the XRD measurements (Fig. S13) and AFM-based surface characterization (Fig. S17). In the first case, we compare the XRD patterns of cysteine powder and thin film (deposited under our experimental conditions on glass substrates from  $10^{-4}$  and  $10^{-6}$  M methanol solutions), however, no cysteine-related peaks from of spin-coated thin films were observed. Additionally, AFM measurements show the overall conservation of the initial surface morphology (and phase images) inside the shuriken structure, which indicates that the cysteine layer homogeneously copies the original metal surface and does not produce any polycrystalline structure.

Finally, we compare the SERS (measured on S3/Ag substrates) and Raman (measured using 785 nm excitation of cysteine bulk) spectra. Obtained results are shown in Fig. S18, while the peaks affiliation is given in Table S1. As could be expected, the SERS and Raman spectra differ, the difference indicating that in the case of S3/Ag substrate, we deal with the real surface enhanced Raman signal.

**Table S1.** Assignment of cysteine (bulk) Raman peaks and cysteine SERS peaks (measured on S3/Ag structure).<sup>S4-S8</sup>

Cysteine powder	Cysteine on S3/Ag	Assignment	Comment
Raman shift, $\text{cm}^{-1}$			
1575	1577	bend $\text{NH}_3^+$ , asym str $\text{COO}^-$	Not intensive on Raman spectra
1424	1421	sciss $\text{CH}_2$	
1397	1372	sym str $\text{COO}^-$ , bend C-H	
1345	1342	bend asym NH	
1292	1286	$\text{CH}_2$ wag	
1200	1154	$\text{CH}_2$ twist	
	<b>1118</b>	<b>C-C str, rock <math>\text{NH}_3^+</math>, str C-N</b>	Not intensive on Raman spectra
1063	<b>1044</b>	<b>Rocking vib <math>\text{NH}_3^+</math></b>	Not presented on Raman spectra
938	994	NH rock	
865	-	CC str	Not possible to recognize on SERS spectra
820	-	$\text{COO}^-$ wag	

770	785	CH <sub>2</sub> rock	
688	-	CS str	Not possible to recognize on SERS spectra
636	633	CS str	
532	-	COO <sup>-</sup> rock	Not possible to recognize on SERS spectra
440	444	CCN bend	

**Table S1 – related discussion**

The comparison of Raman spectra of cysteine with SERS spectra measured on S3/Ag structure indicate the changes of ration of peaks unveiling the adsorption side of cysteine to Ag. NH<sup>3+</sup>, COO<sup>-</sup> and C-N related bands undergo significant changes, while C-S related band did not demonstrate any. This spectral difference suggests that cysteine molecules are adsorbed simultaneously through carboxylate and amino groups functional groups not thiol as was reported for Au and AgNPs<sup>S4</sup>.

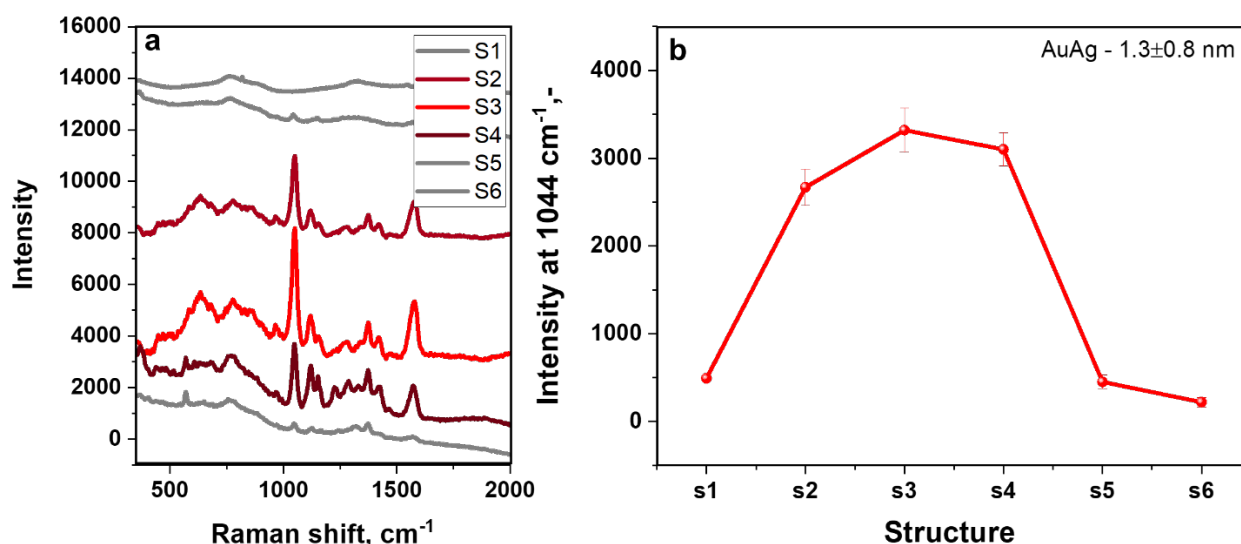


**Fig. S20.** Dependence of SERS signal intensity at 1044 cm<sup>-1</sup> measured from L-Cysteine (10<sup>-4</sup> M) on RH/Ag shurikens geometry at the silver effective thickness of 1.3 nm

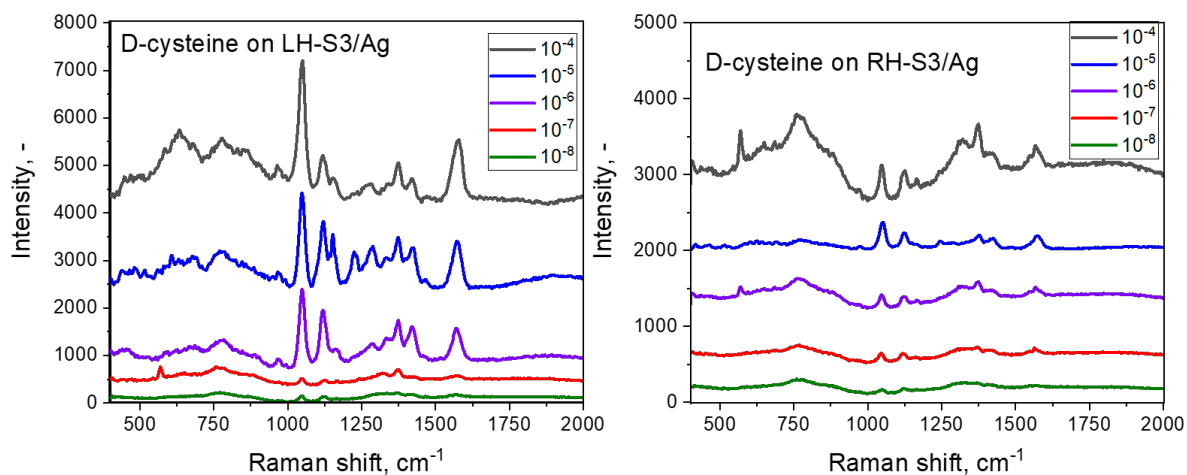


**Fig. S21** SERS spectra of D-cysteine (deposited from  $10^{-4}$  to  $10^{-8}$  M, methanol solution) on LH- or RH-S3/Ag substrates.

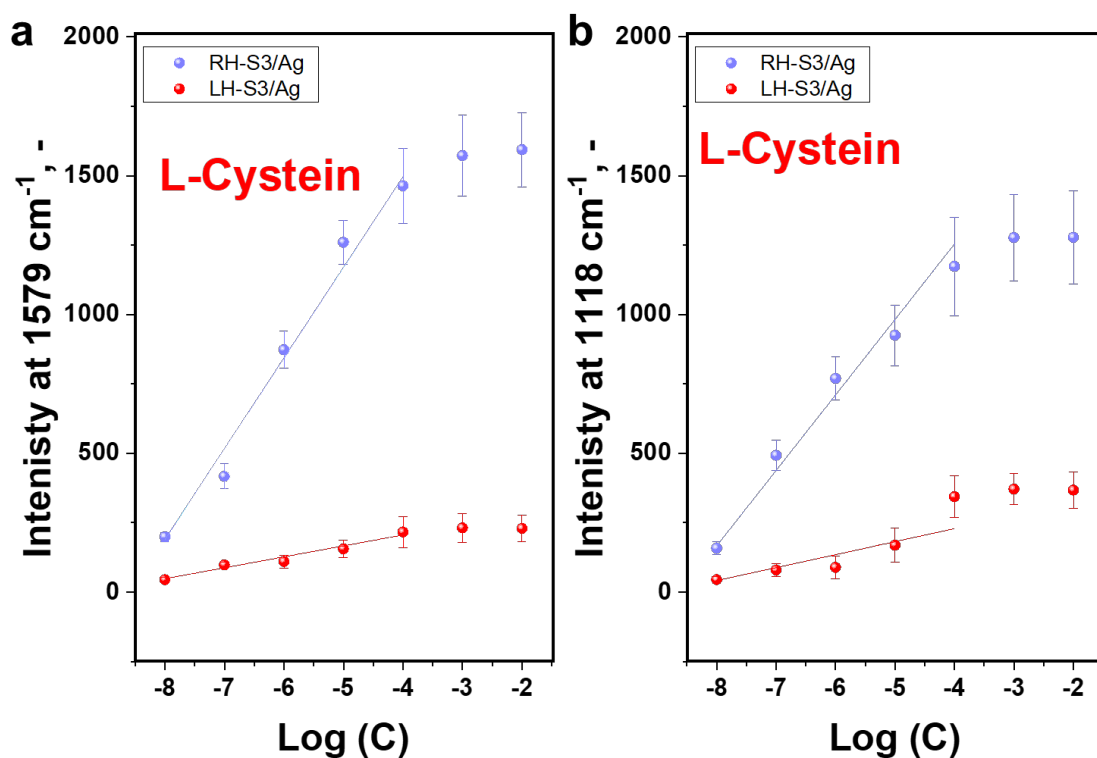


**Fig. S22** The characteristic L-cysteine and D-cysteine SERS band at (a),  $1579 \text{ cm}^{-1}$  and (b)  $1118 \text{ cm}^{-1}$  intensity as a function of the initial enantiomers concentrations and plasmonic substrate LH- or RH- kind.

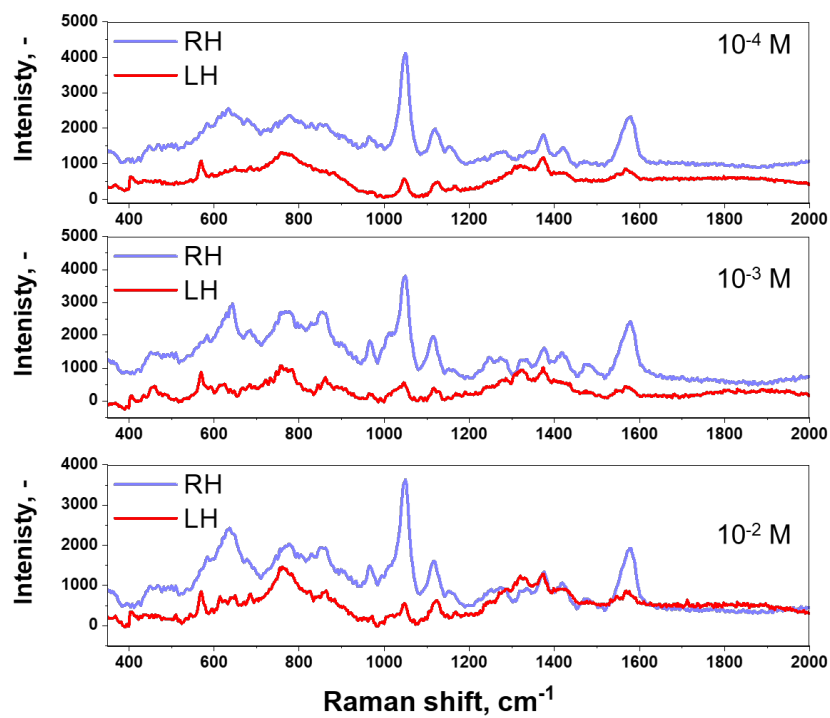


**Fig. S23.** SERS spectra of L-cysteine enantiomer deposited on LH- or RH-S3/Ag substrates from methanol solutions with various initial concentrations ( $10^{-4}$  -  $10^{-2}$  M range)

## 8. SERS PROBE WAVELENGTH PROOF OF AG – SHURIKEN PLASMONIC COUPLING.

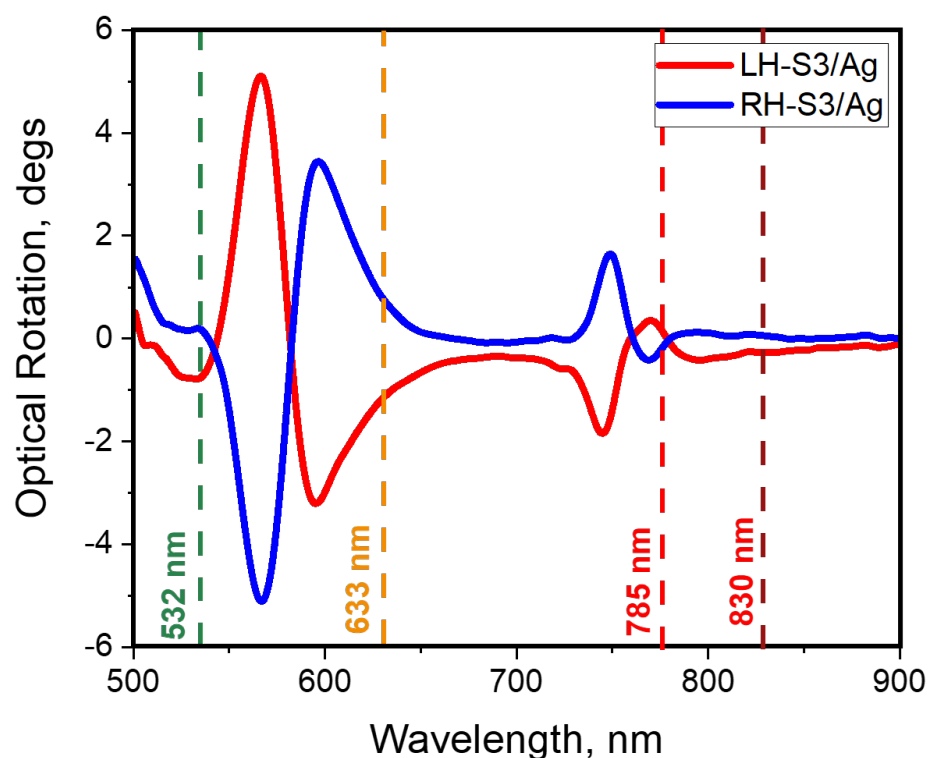


**Fig. S24** Comparison of S3/Ag optical rotation and laser wavelength used for SERS spectra collection.

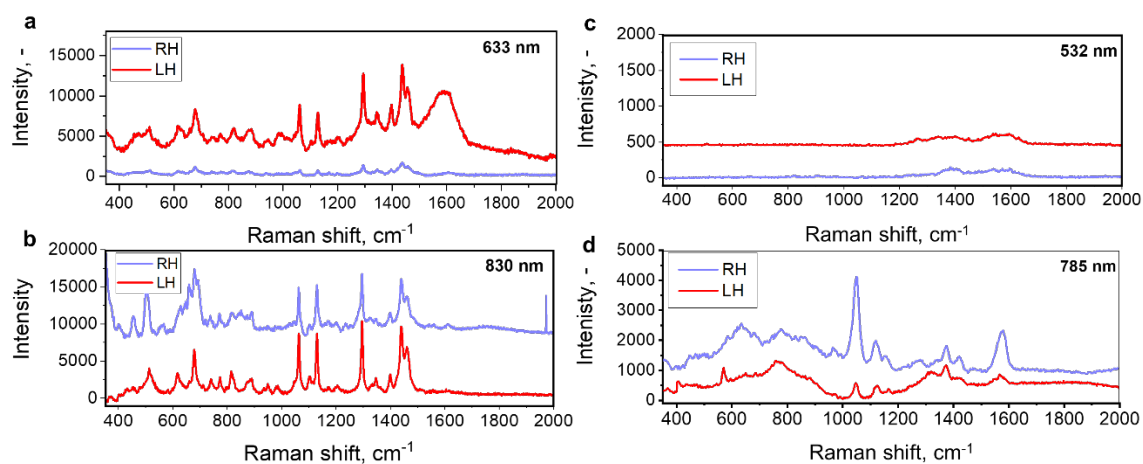


**Fig. S25** SERS spectra of  $10^{-4}$  M L-cysteine deposition of RH/LH-S3/Ag measured with (a) - 633 nm and (b) - 830 nm, (c) - 532 nm, (d) - 785 nm excitation wavelengths

For the sake of clarity, Fig. S24 shows the overlapping of different excitation wavelengths with the ORD of LH/RH-S3/Ag. The excitation at 785 nm wavelength displays an apparent difference in L-cysteine SERS response as a function of shuriken rotation (Fig. S25). In contrast, utilization of 830 and 530 nm did not lead to the difference between spectra on both kinds of substrates (LH-S3/Ag vs. RH-S3/Ag). More interestingly, the 633 nm excitation wavelength also produces a difference – the chiral response is flipped compared to the SERS response at 785 nm excitation. The observed results are consistent with the optical rotation for LH and RH shurikens structures (Fig. S4).

## 9. ANALYSIS OF MIXTURES AND SERS SUBSTRATE RE-UTILIZATION.

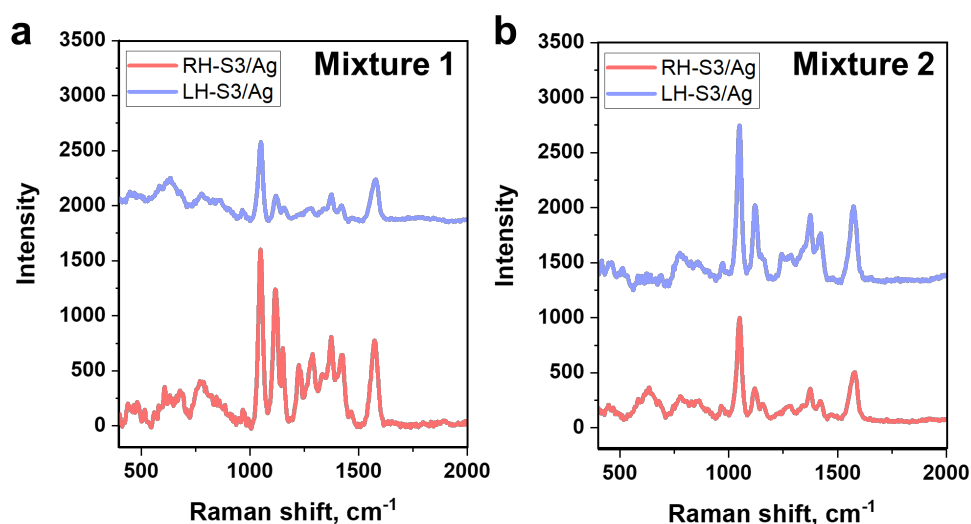


**Fig.S26.** SERS spectra from the mixtures (a) L-Cystein (10<sup>-6</sup> M) and D- Cystein (10<sup>-7</sup> M) and (b) L-Cystein (10<sup>-7</sup> M) and D- Cystein (10<sup>-6</sup> M) measured on RH/LH-S3Ag

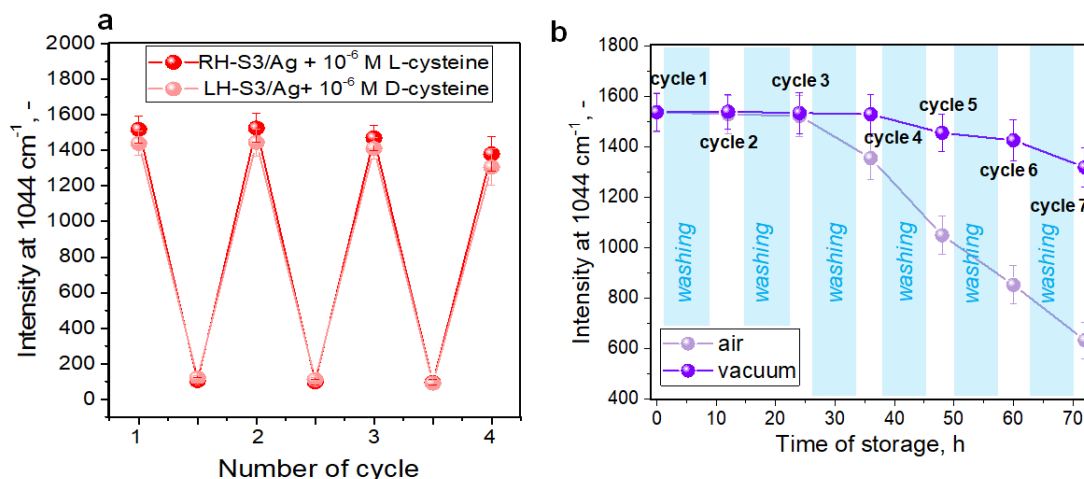


**Fig. S27** (a) – the variation of the intensity of characteristic cysteine SERS band ( $1044\text{ cm}^{-1}$ ), measured in several subsequent cycles of substrates utilization/regeneration (all experiments were performed during one day); (b) - the variation of the intensity of characteristic L-cysteine SERS band ( $1044\text{ cm}^{-1}$ ) measured on RH-S3/Ag after several cycles of substrates utilization/regeneration with additional samples storage in air or vacuum.

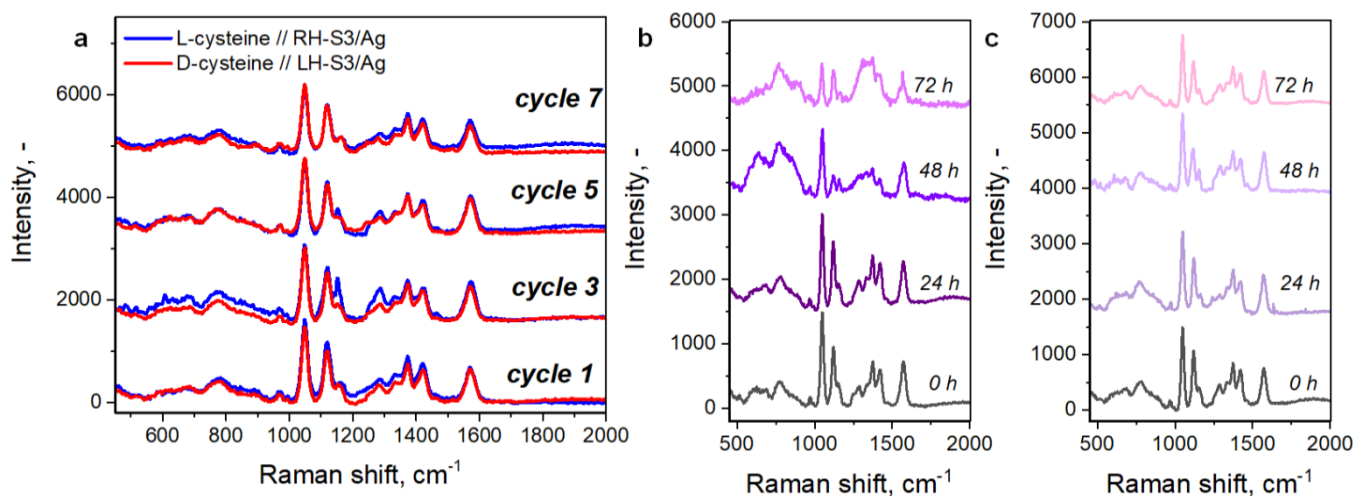


**Fig. S28** (a) - SERS spectra of cysteine enantiomers measured on RH- and LH-S3/Ag substrates after several subsequent cycles of SERS substrates regeneration/re-utilization; (b) - SERS spectra of cysteine enantiomer, measured after several cycles of substrate re-utilization and intermediate storage in the air; (c) - SERS spectra of cysteine enantiomer, measured after several cycles of substrate re-utilization and intermediate storage in a vacuum.

## 10. BIOMOLECULES EXPERIMENTS – DNA CASE

### *Evaluation of potential increase of substrate RH/LH-S3/Ag temperature using molecular probe.*

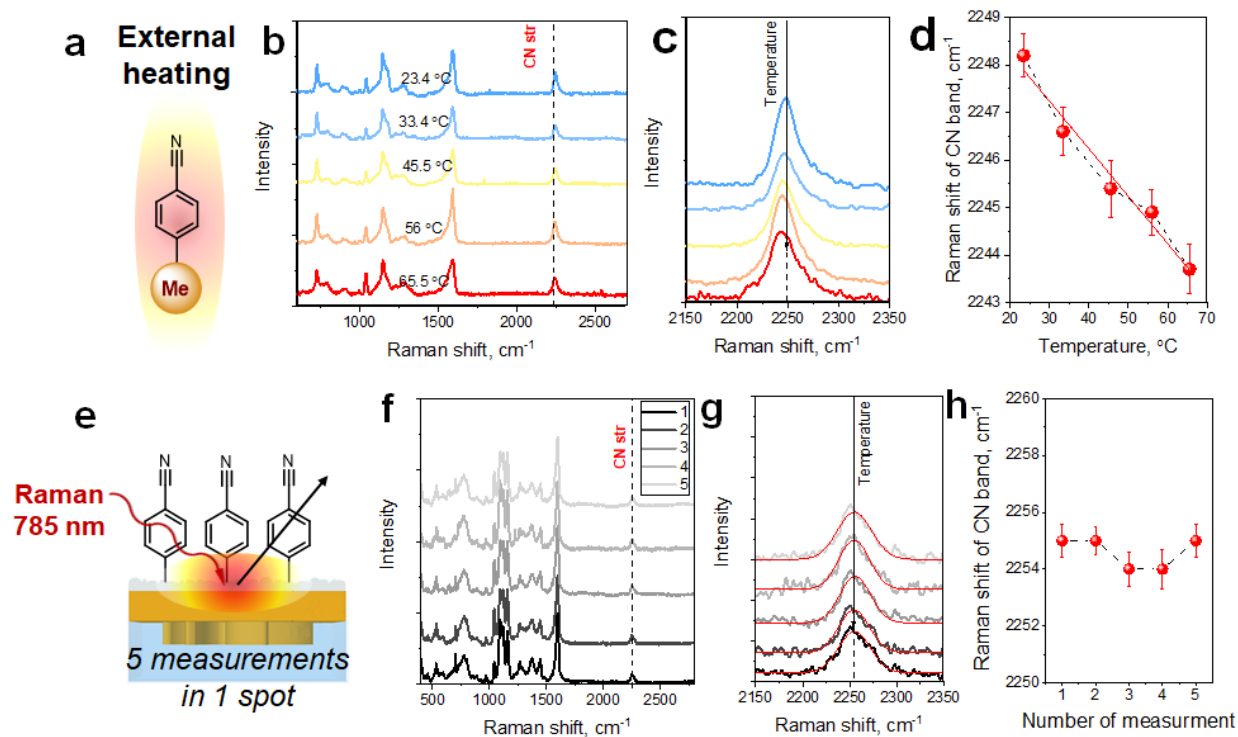


**Fig. S29** (a) - structure of AuNPs-C≡N; (b) - SERS spectra of AuNPs-C≡N under external heating, (c) - magnified region (2150-2350 cm<sup>-1</sup>) for SERS spectra on (b); (d) - dependence of C≡N stretching vibration position on the external temperature; (e) - schematic representation of SERS measurements on RH/LH-S3/Ag-C≡N; (f) - SERS spectra of RH/LH-S3/Ag-C≡N measured in the same point; (g) - magnified region (2150-2350 cm<sup>-1</sup>) for SERS spectra on (f); (h) - dependence of C≡N stretching vibration position on the number of measurements.

### **Fig. S29 – related discussion**

For the evaluation of local surface temperature, we used the changes of C≡N stretching vibration position. It is known that C≡N groups are able to probe the changes in the environment, including temperature changes.<sup>S9,S10</sup> For this task, the plasmon-active substrates were covalently modified by 4-cyanodiazonium tosylate (ADT-CN) to attach C≡N probing groups (Me-C≡N) (Fig. S29a). SERS spectra of grafted organic moieties (Fig. S29b) reveal

peaks at 2250  $\text{cm}^{-1}$  ( $\text{C}\equiv\text{N}$  str vib), 1596  $\text{cm}^{-1}$  ( $\text{C}=\text{C}$  str vib), 1284, 1152, 1042  $\text{cm}^{-1}$  ( $\text{C}-\text{H}$  in plane str vib), 726  $\text{cm}^{-1}$  ( $\text{C}-\text{H}$  out of plane str vib). Grafted plasmon-active substrates were subsequently subjected to SERS measurements at elevated temperatures (Fig. S29b,c). An apparent shift of  $\text{C}\equiv\text{N}$  stretching vibration position was observed with the increase of temperature up to 65.5  $^{\circ}\text{C}$  (Fig. S29c). Observed shift allows to create a calibration curve for local substrate temperature estimation, presented in Fig. S25d). In the next step, several continuous SERS measurements were performed on RH/LH-S3/Ag substrates at RT, also modified by the same ADT-CN. Results are presented in Figs. S25e-h and clearly indicate that 5 sequential SERS measurements did not result in considerable changes in the position of  $\text{C}\equiv\text{N}$  stretching vibration. So, we can conclude that under our experimental conditions there is no significant local heating of the sample surface, which could lead to the changes in DNA structure.

**Table S2** SERS peaks assignments of double-stranded DNA (CGCCAATACGACCAAATCCG-GCGGTTATGCTGGTTTAGGC) deposited on (L/R)-S3/Ag

Peak position, $\text{cm}^{-1}$	Assignment
1690, 1602	C=O str
1543	Adenine, guanine
1455	Heterocyclic ring C=N str
1350	Adenine
1315	Adenine, guanine
1212	Thymine, cytosine
1153	P=O sym str
1111	P=O sym str, C-O str
970	Thymine, cytosine
750	Adenine
595	Guanine

## REFERENCES

---

- [S1] Guselnikova, O.; Postnikov, P.; Elashnikov, R.; Trusova, M.; Kalachyova, Y.; Libansky, M.; Barek, J.; Kolska, Z.; Svorcik, V.; Lyutakov, O. Surface modification of Au and Ag plasmonic thin films via diazonium chemistry: Evaluation of structure and properties. *Colloids Surfac. A*, **2017**, *516*, 274-285.
- [S2] Karimullah, A. S.; Jack, C.; Tullius, R.; Rotello, V. M.; Cooke, G.; Gadegaard, N.; Barron, L. D.; Kadodwala, M. Disposable plasmonics: plastic templated plasmonic metamaterials with tunable chirality. *Adv. Mater.* **2015**, *27*, 5610-5616.
- [S3] Kelly, C.; Tullius, R.; Laphorn, A. J.; Gadegaard, N.; Cooke, G.; Barron, L. D.; Karimullah, A. S.; Rotello, V. M.; Kadodwala, M. Chiral plasmonic fields probe structural order of biointerfaces. *J. Am. Chem. Soc.* **2018**, *140*, 8509-8517.
- [S4] Choi, J. S.; Cho, M. Limitations of a superchiral field. *Phys. Rev. A*, **2012**, *86*, 063834.
- [S5] Yao, G.; Huang, Q. DFT and SERS Study of l-Cysteine Adsorption on the Surface of Gold Nanoparticles. *J. Phys. Chem. C*, **2018**, *122*, 15241-15251.
- [S6] Cuiyu, J.; Fang, Y. Experimental (SERS) and theoretical (DFT) studies on the adsorption behaviors of L-cysteine on gold/silver nanoparticles. *Chem. Phys.* **2007**, *332.1*, 27-32.
- [S7] Guohua, Y.; Qing, H. DFT and SERS Study of l-Cysteine Adsorption on the Surface of Gold Nanoparticles. *J. Phys. Chem. C*, **2018**, *122.27*, 15241-15251.
- [S8] Kuang, X.; Ye, S.; Li, X.; Ma, Y.; Zhang, C.; Tang, B. A new type of surface-enhanced Raman scattering sensor for the enantioselective recognition of D/L-cysteine and D/L-asparagine based on a helically arranged Ag NPs@ homochiral MOF. *Chem. Comm.* **2016**, *52*, 5432-5435.
- [S9] Weeks, C. L.; Polishchuk, A.; Getahun, Z.; DeGrado, W. F.; Spiro, T. G. Investigation of an unnatural amino acid for use as a resonance Raman probe: detection limits and solvent and temperature dependence of the  $\nu_{\text{C}\equiv\text{N}}$  band of 4-cyanophenylalanine. *J. Raman Spectrosc.* **2008**, *39*, 1606-1613.
- [S10] Huang, C. Y.; Wang, T.; Gai, F. Temperature dependence of the CN stretching vibration of a nitrile-derivatized phenylalanine in water. *Chem. Phys. Lett.*, **2003**, *371(5-6)*, 731-738.